PREDICTING NEAR-BED SEDIMENT TRANSPORT THROUGH PARTICLE IMAGE VELOCIMETRY

Caroline Hoch[1], Robert J. Weaver[1], Bret Webb[2], Don Resio[3], Nikole Ward[4], Caleb Lodge[5], Olivia Hopkin[6], and Ruby Bouhassira[7], Nezamoddin N. Kachouie[8]

Coastal communities are growing globally, promoted by the ocean's abundant opportunity for food, recreation, tourism, and green energy. Erosion and accretion along the coast significantly affect the safety of these communities and longevity of coastal infrastructure. To better predict rates of erosion and accretion, sediment transport models and active-bed thickness prediction techniques are of particular importance. Two dimensionless parameters, the Shields and Ursell parameters, are often used to predict rates of sediment transport and wave linearity. The goal of this project is to analyze sediment movement in a laboratory wave flume using particle image velocimetry (PIV). From the analysis we estimate the dimensionless parameters and instantaneous active-bed thickness to predict volumetric sediment transport rates as waves propagate shoreward.

INTRODUCTION

Coastlines are dynamic environments, subject to erosion and sediment transport, characterized by the relationship between waves, currents, tides, and seabed morphology (Dronkers 2005). Coastal erosion can become hazardous in densely populated areas, threatening coastal infrastructure and economic activities (Barnes et al. 2015). In 2020, approximately 3 billion people lived within 200 kilometers of a coastline. It was predicted this number will double by 2025 (Valdenarro 2020). To protect the growing coastal population, accurate techniques for predicting shoreline changes are needed. While long-shore sediment transport is primarily driven by wave-induced currents, cross-shore sediment transport is driven by wave-induced hydrodynamics and undertow (Dean & Dalrymple 2002). Two dimensionless parameters, the Shields and Ursell parameters, are often used to predict sediment motion based on incoming wave properties; however, the detailed behavior and consistency of cross-shore sediment transport is not fully characterized (Mariño-Tapia et al. 2007). This study aims to use particle image velocimetry (PIV) to compare in-situ measurements of velocity and active-bed thickness to the Shields and Ursell parameters. The relationship derived between observed sediment transport and the dimensionless parameters will further understanding of near-bed morphodynamics and provide insight into improving methods of estimating near-shore sediment transport.

Sediment Movement

Waves go through considerable transformations as they propagate towards the shoreline. As deep-water waves approach the shoreline and enter shallower water, they begin to interact with the ocean floor, known as shoaling. The interaction with the ocean floor increases wave height and steepness, driving an increase in water particle orbital velocities. The increase in orbital velocity increases shear stress on the seabed, resulting in sediment motion (Stachurska & Staroszczyk 2019). To determine the influence of sediment characteristics on water and bed movement, A.F. Shields conducted wave flume studies in 1936 (Shields 1936). The Shields parameter has since been used to predict regimes of sediment motion; however, the application of the Shields parameter in literature has been scrutinized for inconsistencies (Buffington 1999). The Shields parameter is the ratio of mobilizing hydraulic

[1] Department of Ocean Engineering and Marine Sciences, Florida Institute of Technology, 150 W. University Blvd., Melbourne, Florida, 32901, United States
[2] Department of Civil, Coastal, and Environmental Engineering, University of South Alabama, 150 Student Services Drive, Mobile, Alabama, 36688, United States
[3] Taylor Engineering Research Institute, University of North Florida, 1 UNF Drive, Jacksonville, FL 32254
[4] Tayor Engineering Research Institute, University of North Florida, Jacksonville, FL and University of Florida, Gainesville, FL
[5] U.S. Army Corps of Engineers, Los Angeles District, 915 Wilshire Blvd, Los Angeles, CA 90017
[6] Brigham Young University, Provo, UT 84602, United States
[7] Haverford College, 370 Lancaster Ave, Haverford, PA 19041, United States
[8] Department of Mathematical Sciences, Florida Institute of Technology, 150 W. University Blvd., Melbourne, FL 32901, United States

loading forces to the stabilizing gravitational force on sediment particles (Roulund et al. 2016). This value is dependent on grain size and roughness, which effect both hydraulic loading and stabilizing forces. It is assumed that bed movement begins at Shields values of 0.05, sand ripples develop and are stable at values of 0.2 to 0.3, and mass sediment movement occurs at values 0.8 to 1.0 (Stachurska & Staroszczyk 2019).

Wave Linearity

As waves move shoreward and begin to shoal, they increase in nonlinearity. In the shallow water region, wavelengths become much larger than water depth and linear wave theory is no longer applicable (Svendsen 2006). Under nonlinear waves, the wave crest phase produces much higher values of velocity and shear stress than under the trough. Consequently, the net sediment transport rate is primarily driven by the wave crest phase under nonlinear waves. As the waves approach the shore and become more nonlinear, the net sediment transport increases (Ostrowski 2018). Determining the region of linearity for the waves is critical for accurately calculating net sediment transport, as different mathematical theories are applicable for specific regions. The Ursell number can be used to classify the region of linearity and is defined as the ratio of wave height and wavelength squared to water depth cubed (Hedges 1995).

Waves can be classified as linear shallow water waves, Stokes wave (of varying order), cnoidal waves, or solitary waves. Linear water wave theory assumes that the wave steepness is so small that the nonlinear effects of the free surface can be neglected. Stokes second and higher order wave theory is used to describe weakly nonlinear waves with small wave steepness, but is not applicable for cnoidal or solitary waves, as illustrated in Fig. 1 (Svendsen 2006; Hedges 1995). Cnoidal and solitary waves have relative depths smaller than that assumed by Stokes wave theory. Ursell numbers less than 40 indicate linear waves or Stokes waves, while values between 40 and 4000 indicate cnoidal waves. Values greater than 4000 indicate solitary waves (Hedges 1995).
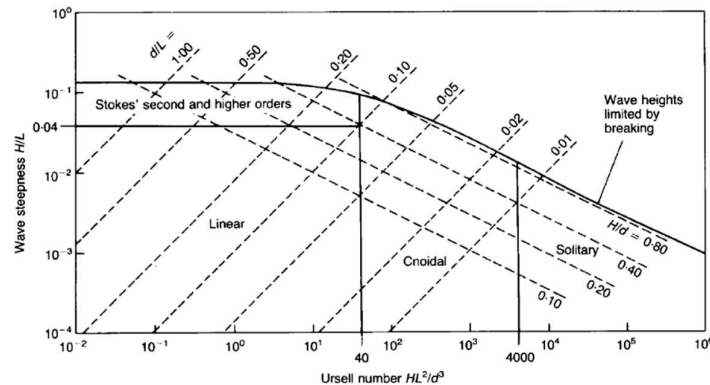

Figure 1. Regions of Validity for Wave Theories (Hedges 1995)

Cnoidal wave theory is an explicit theory for shallow water waves. It is not widely applied due to its reliance on the complicated Jacobian elliptical functions; however, it gives an analytical solution for weakly nonlinear waves more accurately than that of linear wave theory (Fenton & Herbich 1998; Svendsen 2006).

Particle Image Velocimetry

Particle image velocimetry (PIV) is a measurement method that was developed in the 1980s and is often used in fluid mechanics to qualitatively analyze fluid flow (Raffel et al. 2018). PIV directly measures both time and displacement of scattered particles and uses the particles as markers of fluid motion. PIV is unique in the sense that it gives entire velocity fields of the fluid, as opposed to one singular point when measured with gauges. This provides the user the ability to see instantaneous flow patterns that may be missed with single-point measurements. An additional benefit to the use of PIV over single-point probes is that PIV is non-intrusive. While gauges need to be inserted into the fluid

flow, PIV analysis relies on optical techniques which do not disrupt fluid flow (Adrian & Westerweel 2011).

The experimental setup for PIV relies on multiple subsystems, including seeding, illumination, recording, calibration, evaluation, and post-processing. Seeding refers to the addition of tracer particles into the flow for adequate laser illumination (Raffel et al. 2018). For this study, the sediment size was large enough that laser illumination was sufficient, and the addition of tracer particles was not required since the system was being used to track particles not track the flow. The illumination subsystem requires that the particles of interest be illuminated at least twice within a short, predetermined time interval to allow for calculations of displacement. Recording is required for PIV analysis so that frame by frame analysis can be conducted following the trial. For this study, a high-frame rate camera was utilized to capture sediment motion over the duration of the waves. PIV systems need to be accurately calibrated to measure displacement over time when compared to the image plane. The evaluation subsystem calculates particle displacement by analyzing the consecutive image frames. Cross-correlation between the first and second illumination of a particle occurs within small interrogation areas to determine the local displacement vector. The final subsystem, post-processing, is where the user removes invalid measurements and extracts parameters of interest (Raffel at al. 2018). For this study, PIVlab within MATLAB was used for PIV evaluation, pre-processing, post-processing, and extraction.

Pre-processing allows the user to adjust the image with a variety of filters prior to analysis to enhance the quality of the image and reduce invalid vectors. Contrast limited adaptive histogram equalization (CLAHE) operates in small regions of the image where the most frequent intensities of the image histogram are spread throughout the region. This optimizes low and high exposure regions independently and increases the probability of detecting valid vectors. Lighting within the PIV setup can cause low-frequency illuminations in the background information of images. The high pass filter suppresses low-frequency information, including displacements, and focuses the image on the high-frequency illumination of the sediment. (Thielicke & Stamhuis 2014).

Within the pre-processing stage of PIV analysis, the user can specify the cross-correlation algorithm. The cross-correlation algorithm is a statistical technique that aims to derive the most accurate particle displacement within the interrogation areas. The cross-correlation algorithm can either be discrete cross correlation (DCC), or discrete Fourier Transform (DFT). With DCC, the interrogation areas between two images can be different sizes and the correlation matrix is computed within the spatial domain. It has been shown to create more accurate results than the DFT algorithm; however, it is more computationally expensive. The DFT algorithm calculates the correlation matrix within the frequency domain using a fast Fourier Transform (FFT). With FFT, the interrogation areas of two images need to be the same size. To offset the lower accuracy of FFT, multiple passes with offset interrogation areas can be implemented which increases spatial resolution. Between passes velocity data is smoothed and validated, resulting in highly accurate final velocities for the interrogation area (Thielicke & Stamhuis 2014).

Within the pre-process settings, the user must specify the desired peak finding and sub-pixel estimation techniques. The displacement of a particle between two interrogation areas can be determined by identifying the peak intensity within the correlation matrix. This peak is then adjusted by fitting a Gaussian function to the intensity distribution by using adjacent vertical and horizontal pixels. The peak of the newly fitted function is used to find the particle displacement. A graphical representation of this process is included in Fig. 2 (Thielicke & Stamhuis 2014).
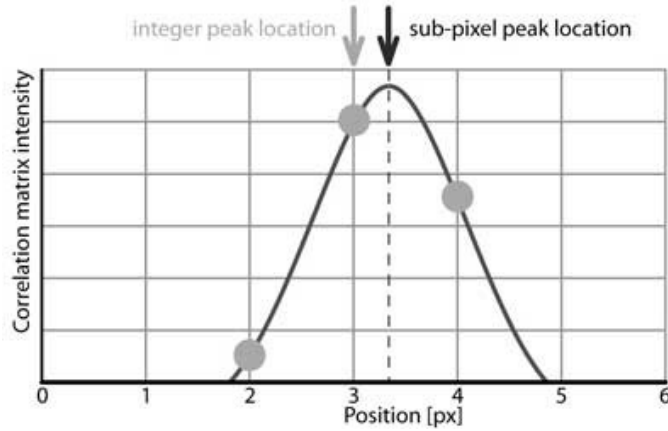
Figure 2: Gaussian 2x3 Intensity Distribution (Thielicke & Stamhuis 2014)

If the displacement peak has an elliptical shape, a two-dimensional Gaussian function should be utilized; however, the benefit of utilizing the two-dimensional Gaussian function is more noticeable with single-pass DFT and DCC methods.

There are three options for correlation robustness within PIVlab: standard, high, and extreme. These methods are differentiated by their cross-correlation and interpolation methods. Circular cross-correlation assumes the image data to be periodic, while linear cross-correlation does not. Linear cross-correlation may produce higher quality displacement estimates; however, it is more computationally expensive. The two types of interpolation methods are bilinear, which is faster, and spline, which has higher precision. The standard robustness method uses linear window deformation and circular correlation. The high robustness method uses spline window deformation and linear cross-correlation. The extreme correlation robustness method uses repeated linear cross-correlation and spline window deformation. (Thielicke & Sonntag 2021).

Post-processing settings allow the user to set the limits for data validation. Applicable post-processing settings for this study include setting velocity vector limits, a standard deviation filter, a local median filter, and a low-contrast filter. Velocity vector limits can be set manually by selecting the valid velocity area within the PIVlab generated scatterplot. The standard deviation filter and local median filter work to semi-automatically limit velocity vectors. The standard deviation filter compares each velocity vector with a lower and upper threshold, where $\bar{\mu}$ is the mean velocity and σ_μ is the standard deviation of the mean velocity. The user selects the value for n, which determines the limits of this filter, as shown in Equation 1 and 2 (Thielicke & Stamhuis 2014).

$$U_l = \bar{\mu} - n \cdot \sigma_\mu \qquad\qquad (1)$$
$$L_l = \bar{\mu} + n \cdot \sigma_\mu \qquad\qquad (2)$$

The local median filter works in a similar fashion to the standard deviation filter; however, it compares each velocity fluctuation to the median in a 3 by 3 grid surrounding a central vector (Thielicke & Stamhuis 2014).

The low-contrast filter is unique from the other post-processing filters discussed as it filters data based on the input image, as opposed to the velocity vectors. The low-contrast filter removes vectors in regions with low contrast, often caused by shadows and areas without illuminated particles.

PIVlab allows the user to extract and process data in a multitude of ways. For this study, a polyline to define a coordinate line of interest was manually drawn and used to extract u-component velocity vectors. Within PIVlab, the user can visually assess the velocity vectors with a PIVlab generated x-y plot. These plots and associated data can then be saved out as a text file to the desktop.

METHODOLOGY

Wave Flume Studies

The South Alabama wave-current flume was utilized to model the beach profile of Duck, North Carolina at a 1:16 scale. The wave-flume is 17.5-meters long, 1.5-meters wide, and 1.0-meters deep. A piston wave maker is located on the upstream end of the wave-current flume which allows the user to specify the desired frequency of waves. Two control pumps are located at the down-stream end of the wave-current flume, capable of circulating water through the wave-flume at rates up to 100 liters per second. Glass panels line either side of the wave-current flume, allowing the user to observe flow conditions and sediment motion throughout the flume.

Sediment was obtained from Smith Sand in Eight Mile, Alabama. The results of a standard sieve analysis indicate that the median grain size was 0.31 mm, which was used as d_{50} in applicable calculations.

Capacitance wave gauges were used to record the time series of the surface at seven locations along the profile. Five regular waves and six irregular sets of waves were simulated in the wave-current flume. For each trial, the time series of surface elevation was plotted and used to measure wave period, T, and wave height, H, for the wave of interest. Wave period was measured as the time difference between the crest of interest and preceding crest. Wave height was taken as the distance between the crest of interest and preceding trough. A typical plot is included as Fig 3. Wave characteristics for the eleven trials are included in Table 1.
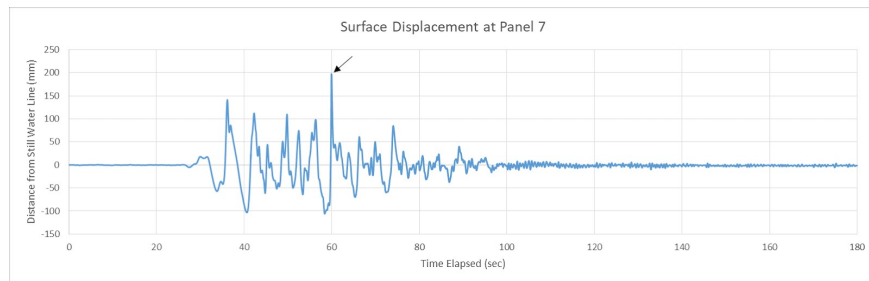

Figure 3: Typical Surface Displacement Plot. The black arrow indicates crest of interest.

Table 1: Wave Properties of Wave Simulation Trials			
Regular Waves			
Panel Label	Water Depth (meters)	Wave Height (meters)	Period (seconds)
P05	0.250	0.188	3.063
P06	0.365	0.319	2.875
P07	0.430	0.274	2.938
P08	0.375	0.235	2.950
P09	0.425	0.600	3.000
Irregular Waves			
P05	0.265	0.338	5.562
P06	0.385	0.274	5.441
P07	0.450	0.303	5.658
P08	0.385	0.237	4.467
P09	0.440	0.217	2.916
P10	0.465	0.153	4.034

Particle Image Velocimetry

A PIV system was implemented at the wave tank, consisting of a sand-particle illuminating laser, labeled 2 in Figure 4, and high-frame rate camera, labeled 1 in Figure 4. The camera captured the motion of the illuminated sand-particles over the duration of each wave at a frame frate of 1/960th of a second. At each of the seven capacitance wave gauge locations, labeled 4 in Figure 4, high frame rate videos were recorded for analysis in PIVlab.
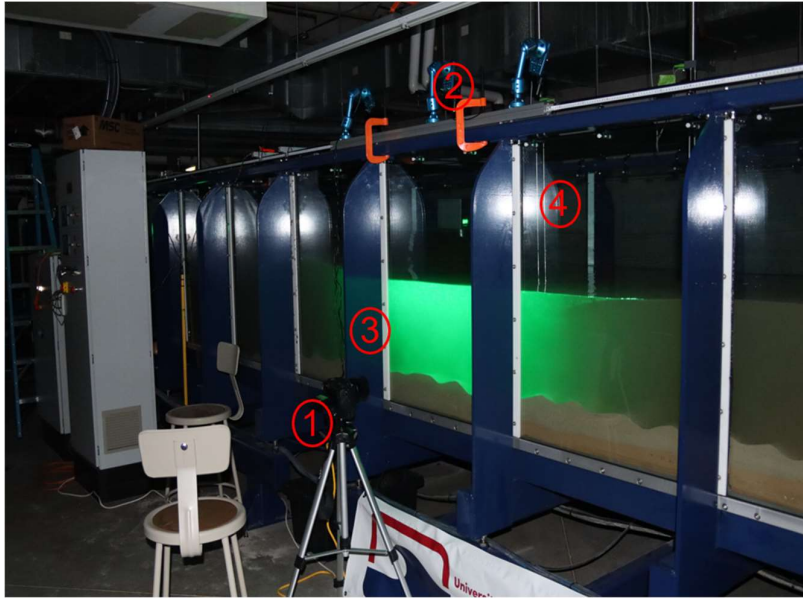

Figure 4: The experimental set-up and PIV system. The system includes a high-frame rate camera (1), lasers (2), the panel of interest, referred to as P##, (3), and wave capacitance gauges (4).

Within PIVlab, each video was calibrated and pre-processed. Pre-process settings were chosen based on developer recommendations, literature reviews, and preliminary testing. Pre-process settings are listed in Table 2.

Table 2: PIVlab Pre-Processing Settings	
CLAHE Window Size (px)	64 (default)
Highpass Kernel Size (px)	10
PIV Algorithm	FFT window deformation (default)
Interrogation Areas (px)	128, 100, 64, 32
Step (px)	64, 50, 32, 16
Sub-Pixel Estimator	Gauss 2x3-point (default)
Correlation Robustness	Standard (default)

Post-processing was performed in PIVlab for each trial. Post-processing values were determined based on preliminary testing. Vectors were compared to the visual assessment of sediment motion, surrounding instantaneous vectors, and the individual velocity variation between frames. Vector velocity limits were chosen to exclude erroneous vectors within the PIVlab generated scatterplot. The low contrast and standard deviation filters were set to 0.0005 and 5, respectively. Regular waves and irregular waves were post-processed with a local median filter of 5 and 3, respectively, except for Irregular Wave P09. Irregular Wave P09 trial had time intervals with poor resolution, and as a result,

the local median filter was increased to 5 to achieve more valid vectors. Vector validity limits are included in Table 3.

Table 3: U-Component Velocity Limits	
Regular Waves	
Panel Label	U-Component Velocity Limits (m/s)
P05	-1.28 to 2.19
P06	-1.15 to 1.18
P07	-1.10 to 1.14
P08	-1.15 to 1.51
P09	-1.15 to 1.51
Irregular Waves	
P05	-1.50 to 1.52
P06	-1.00 to 1.40
P07	-1.44 to 1.72
P08	-1.16 to 1.71
P09	-1.10 to 1.67
P10	-1.45 to 1.67

Following post-processing, a coordinate line was chosen to be applied at each frame for velocity extraction and data analysis. The coordinate line was chosen at ridge locations displaying significant sediment motion and extends from the lower extent of laser illumination into the bed to the upper boundary of the frame. 150 u-component velocities were extracted at each frame and saved as text files for data analysis in MATLAB.

Shields Number Estimates

The Shields parameter is the ratio of mobilizing hydraulic loading forces to the stabilizing gravitational force on sediment particles and is dependent on the mean diameter and particle density (Eq. 3), where U_m is maximum orbital velocity, $f_{2.5}$ is grain roughness friction factor, s is specific gravity, g is gravitational acceleration, and d_{50} is median grain size.

$$\theta = \frac{\frac{1}{2}f_{2.5}U_m^2}{(s-1)gd_{50}} \tag{1}$$

Maximum orbital velocity was taken as the maximum velocity magnitude within the first half centimeter of the coordinate extraction line. The velocities were time-averaged to a 10th of a second. The grain roughness friction factor is dependent on wave orbital amplitude, A. Wave orbital amplitude (Eq. 6) was found by dividing maximum orbital velocity by angular frequency, ω. (Eq. 5). (Masselink et al. 2007; Stachurska & Staroszczyk 2019).

$$f_{2.5} = exp\left[5.213\left(\frac{2.5d_{50}}{A}\right)^{0.194} - 5.977\right] \tag{2}$$

$$\omega = \frac{2\pi}{T} \tag{3}$$

$$A = \frac{U_m}{\omega} \tag{4}$$

The Shields parameter was calculated for every frame at the chosen location for each panel investigated.

Cnoidal Properties and Estimates

The Ursell Number, U_r, is a dimensionless parameter used to assess wave linearity. The Ursell Number was calculated for each wave trial and then assessed for cnoidal properties (Eq. 7).

$$U_r = \frac{L^2 H}{h^3} \tag{5}$$

Within this equation, L is wavelength, H is waveheight, and h is water depth. As the Ursell Number reflects the linearity of the wave, linear properties must first be determined to obtain an initial linear Ursell number. If the linear Ursell number falls within the cnoidal regime, cnoidal wavelength and Ursell number must then be obtained. Linear wavelength, L_L, was found by rearranging the dispersion equation (Eq. 8) to iteratively solve for wavelength. Within this equation, k is wave number (Eq. 9) and L_0 is deep water wavelength (Eq. 10). The rearranged dispersion equation for wavelength iteration is given by Equation 11.

$$\omega^2 = gk\tanh(kh) \tag{6}$$
$$k = \frac{2\pi}{L_L} \tag{7}$$
$$L_0 = \frac{gT^2}{2\pi} \tag{8}$$
$$L_L = L_0 \tanh(\frac{2\pi}{L_L} h) \tag{9}$$

Preliminary values indicate that all trials fell within the cnoidal region (Ursell numbers between 40 and 4000) (Hedges 1995). Therefore, cnoidal wavelength and Ursell number were calculated for each trial. The iterative process outlined by Svendsen in *Introduction to Nearshore Hydrodynamics* was followed (Svendsen 2006). The cnoidal properties are dependent on the elliptical Jacobian functions of the first and second kind. The incomplete elliptical integrals of the first and second kind are given by Equations 12 and 13, respectively.

$$F(\emptyset, m) \equiv \int_0^\emptyset (1 - m\sin^2\theta)^{-\frac{1}{2}} d\theta \tag{10}$$
$$E(\emptyset, m) \equiv \int_0^\emptyset (1 - m\sin^2\theta)^{\frac{1}{2}} d\theta \tag{11}$$

Within these equations, m represents the elliptical modulus and $\emptyset$ is the amplitude. When amplitude is equal to $\frac{\pi}{2}$, the integrals are defined as complete elliptic integrals, given by Equations 14 and 15.

$$K(m) \equiv F(\frac{\pi}{2}, m) \tag{12}$$
$$E(m) \equiv E(K(m), m) \tag{13}$$

The Ursell number may be defined in terms of the elliptical modulus and first complete elliptic integral, shown by Equation 16.

$$U = \frac{16}{3} mK^2(m) \tag{14}$$

To solve the numerical solution of the cnoidal Ursell number, a complimentary parameter was defined (Eq. 17). This leads to redefinition of the Ursell number (Eq. 18).

$$m_1 = 1 - m \tag{15}$$
$$U = \frac{16}{3}(1 - m_1)K^2(m_1) \tag{16}$$

An iteration was then performed by solving wavelength (Eq. 19). For the first iteration, the expression A was assumed to be 1. The expression A is not to be confused with wave orbital amplitude, as used in the calculation of the Shields number.

$$\frac{L}{h} = T\sqrt{\frac{g}{h}} \sqrt{1 + \frac{H}{h} A} \tag{17}$$

Wavelength was then substituted into Eq. 7 to find an Ursell number. This first Ursell number was then used to find an initial complimentary parameter, m_1 (Eq. 20). Approximate coefficients used in the series of equations are listed in Eq. 21.

$$m_1 \sim \exp\left(\frac{a_0 - (\frac{3}{16}U_r)^{\frac{1}{2}}}{b_0}\right) \tag{18}$$

$$a_0 = 1.3862944 \; ; \; b_0 = 0.5$$
$$a_1 = 0.1119723 \; ; \; b_1 = 0.1213478$$

$$a_2 = 0.0725296 \; ; \; b_2 = 0.0288729 \tag{19}$$
$$e_1 = 0.4630151 \; ; \; f_1 = 0.2452727$$
$$e_2 = 0.1077812 \; ; \; f_2 = 0.0412496$$
$$\epsilon = 3 \cdot 10^{-5}$$

The initial complimentary parameter was substituted into Equation 18 and Equations 22 through 26 to find the next parameter in the iteration, $m_{1,i+1}$.

$$K(m_1) = [a_0 + a_1 m_1 + a_2 m_1^2] - [b_0 + b_1 m_1 + b_2 m_1^2] \ln m_1 + \epsilon(m_1) \tag{20}$$
$$\frac{dK}{dm_1} = a_1 + 2a_2 m_1 + [b_1 + 2b_2 m_1] \ln m_1 - [b_0 + b_1 m_1 + b_2 m_1^2] \frac{1}{m_1} \tag{21}$$
$$f(m_1) = 1 - m_1 - \frac{3U}{16K^2} \tag{22}$$
$$f'(m_1) = \frac{3U}{8K^3} \frac{dK}{dm_1} - 1 \tag{23}$$
$$m_{1,i+1} = m_{1,i} - \frac{f(m_{1,i})}{f'(m_{1,i})} \tag{24}$$

This then restarted the iteration process, where $m_{1,i+1}$ was substituted into Equations 22 and 27 as the new elliptical modulus to solve for new complete elliptical functions. These were then plugged into Equation 28 to solve for a new A. The new value of A was plugged into Equation 19 to find a corresponding wavelength. If the initial wavelength and final wavelength differed by more than 0.001, then the iteration restarted with an initial wavelength equal to half the sum of the initial and final wavelength.

$$E(m_1) = (1 + e_1 m_1 + e_2 m_1^2] - [f_1 m_1 + f_2 m_1^2] \ln m_1 + \epsilon(m) \tag{25}$$
$$A(m) = \frac{2}{m} - 1 - \frac{3}{m} \frac{E(m)}{K(m)} \tag{26}$$

The iterative process was coded into MATLAB and the cnoidal Ursell number was calculated for every trial.

Active-Bed Thickness

In order to calculate sediment transport from the PIV data, the volume of sediment moving at the bed must be known. The cross-shore, or x, distance traveled can be extracted as the distance a pixel moves. The y-distance (into the screen) is taken as a unit distance assuming flow is uniform across the tank. The vertical distance needed is the thickness of the active bed. A novel method for calculating active bed thickness was developed. Active bed thickness was calculated through an analysis of pixel intensity. To begin this process, time stacked images were generated for each trial. This process extracted the pixels along the chosen coordinate line for each frame and combined the pixels into one image. This showed the sediment movement at the chosen location over the course of the video in one image. Time stacked images were created for each trial.

Each time stacked image was imported into MATLAB. Time stacked images were originally cropped to eliminate suspended sediment; however, they were later assessed with the entire uncropped image, as discussed in the Results section. The images were then changed into gray scale and an intensity matrix was calculated for the time stacked image. The pixel intensities were smoothed using locally weighted linear regression. For each column in the time stack, representing one frame of the trial, the maximum pixel intensity was identified. To find the upper boundary of the active bed, peaks and troughs of intensity for each column were located. Peaks represent where the laser illumination of sediment is the greatest, while troughs represent areas of little to no laser reflection indicating the absence of particles or in the case of suspended fines, a minimum of particles in the water. For the upper boundary, peaks in pixel intensity were originally defined as those exceeding 40% of the maximum intensity value. The greatest derivative between the first identified peak and the following trough was taken as the upper boundary of the active bed at that location. The lower boundary of the active bed was found using a similar method. Lower boundary peaks were originally identified for each column of pixels that exceed 35% of the maximum intensity value. The greatest derivative between the first peak and the preceding trough was taken as the lower boundary of the temporal bed.

The minimum value of temporal bed thickness for the entire time stacked image was subtracted from the upper boundary to eliminate the static bed. This essentially increased the lower boundary of the active bed, removing thickness values where active bed thickness should be zero. The difference between the adjusted upper and lower boundary of temporal bed thickness was taken as the active bed thickness for each column within the time stacked image.
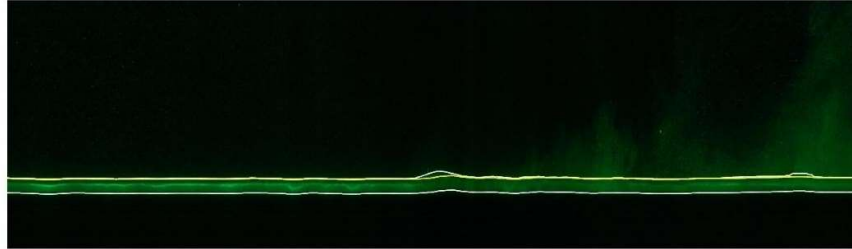

Figure 5: Typical preliminary time stacked image with upper and lower boundary shown in white. Adjusted lower boundary is shown in yellow. Active bed thickness was taken as the upper boundary minus the adjusted lower boundary.

RESULTS

Active-Bed Thickness

It was found that using uncropped time-stacked images and changing the limits for peak identification for the upper active-bed boundary had a significant effect on the active-bed thickness measurements. Using cropped time-stacked images reduces the amount of suspended sediment in the image and is more accurate for comparing instantaneous velocities and instantaneous active-bed thickness. Adjusting the peak definition of pixel intensities from 40% to 60% of the maximum peak and using uncropped images resulted in active-bed thicknesses that were underestimated. This underestimation is apparent through the visual comparison of the Shields number and the active-bed thickness plots, as illustrated in Figures 6. The Shields number and active-bed thickness were time-averaged to a 10th of a second for analysis.
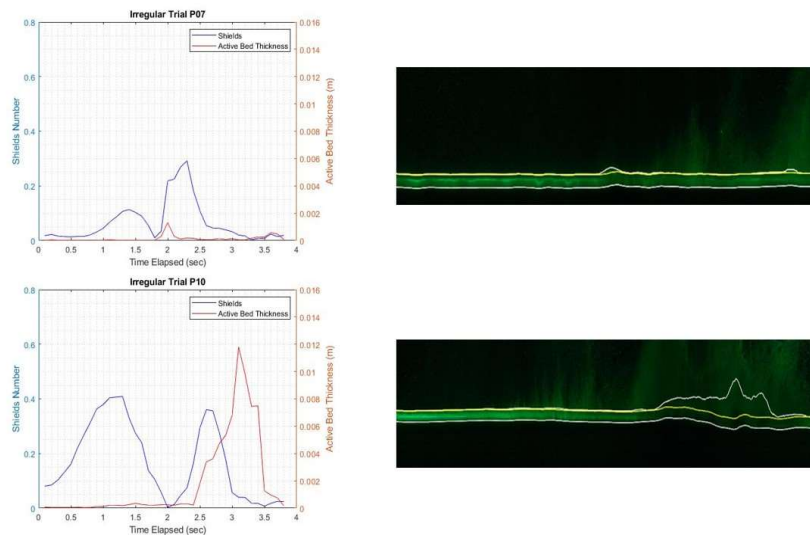

Figure 6: Areas of underprediction of active-bed thickness in Irregular Trials P07 and P10, respectively.

When the upper boundary peak definition was maintained at pixel intensities exceeding 40% of the maximum peak intensity in the cropped image, these areas of underprediction were mitigated. This relationship is illustrated in Figure 7. The resulting plots showed that all wave trials had peaks in Shields number and active-bed thickness occurring at similar times, with some trials showing these peaks skewed only by a few tenths of a second. Plots of remaining trials are shown in Figure 8.
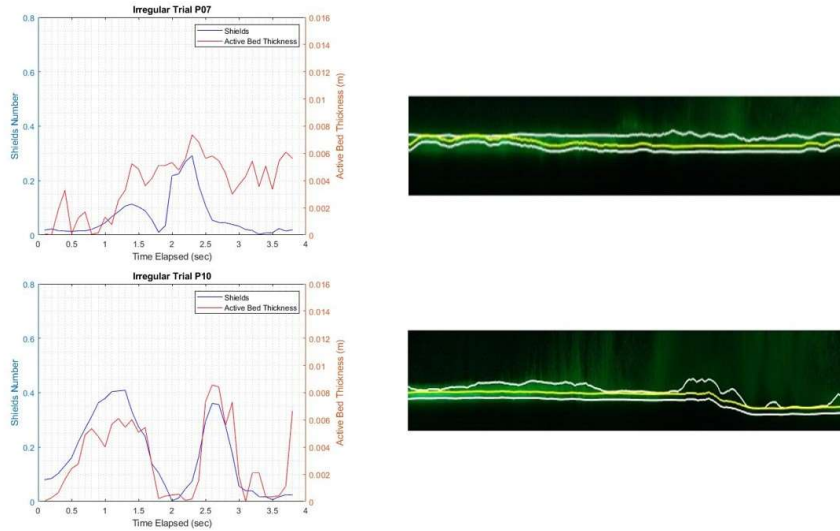

Figure 7: Adjusted active-bed thickness plots for Irregular Trials P07 and P10, respectively.
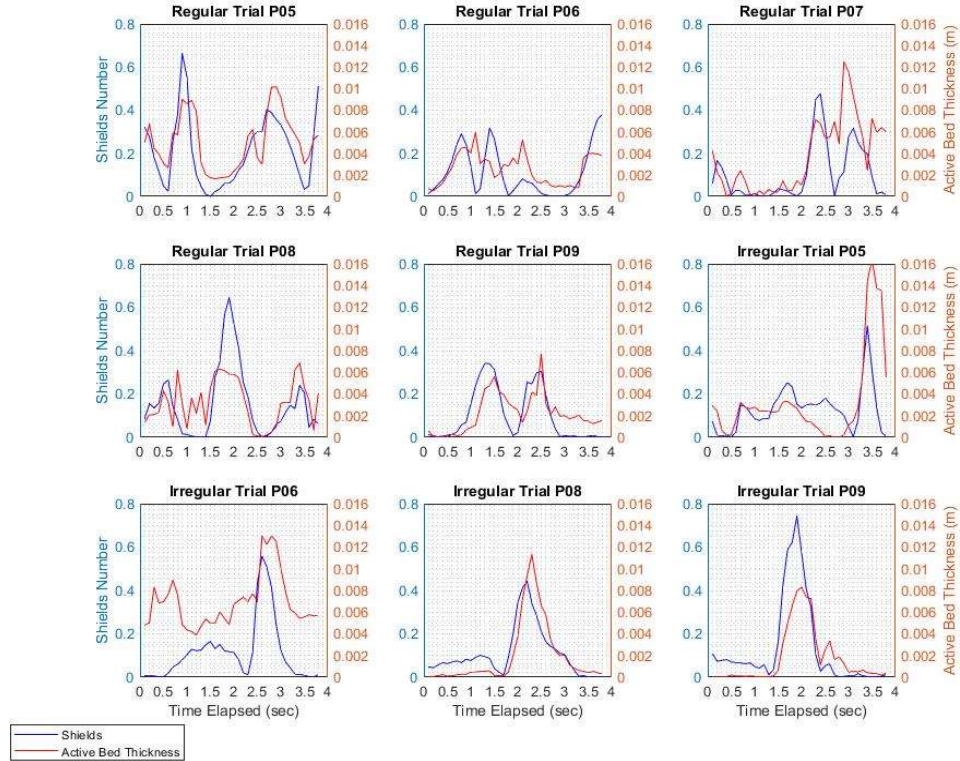

Figure 8: Shields Number vs. Active Bed Thickness

Preliminary Flux Rates

With the active-bed thickness measurements showing promising results, sediment flux rates were calculated for each wave trial. Near-bed velocity was found by averaging the vertically smoothed velocities within 0.5 centimeters of the extent of laser illumination into the bed. For each frame, velocities were vertically smoothed by a moving average with a window of 3 at the point of interest. The average near-bed velocities were then multiplied by the corresponding instantaneous active-bed thickness. The instantaneous sediment movement at that point was found by multiplying the instantaneous flux rate by the time-step for each frame, 1/960th. The net sediment movement at the point of interest was found by summing up the instantaneous movements. The average sediment flux rate was found by then dividing the total movement by the total time of the video. The flux rate for each trial is given in Table 4. Negative flux rates indicate offshore sediment transport while positive flux rates indicate shoreward sediment transport.

Table 4: Preliminary Flux Rates			
Regular Wave Trials			
Trial	Cnoidal Ursell Number	Net Transport (m^3)	Average Flux Rate (m^3/sec)
P05	413.75	$-6.16*10^{-4}$	$-1.59*10^{-4}$
P06	296.17	$-7.09*10^{-4}$	$-1.83*10^{-4}$
P07	161.52	$6.24*10^{-6}$	$1.61*10^{-6}$
P08	186.56	$7.26*10^{-4}$	$1.87*10^{-4}$
P09	85.30	$-1.14*10^{-4}$	$-2.93*10^{-5}$
Irregular Wave Trials			
P05	3086.00	$5.89 * 10^{-4}$	$1.52*10^{-4}$
P06	826.30	$1.70*10^{-3}$	$4.26*10^{-4}$
P07	705.00	$7.48*10^{-4}$	$1.93*10^{-4}$
P08	442.49	$1.40*10^{-3}$	$3.55*10^{-4}$
P09	109.21	$2.30*10^{-3}$	$5.88*10^{-4}$
P10	127.59	$1.56*10^{-4}$	$4.02*10^{-5}$

CONCLUSION

The results of this study indicate that small adjustments of the peak definition in the active bed thickness prediction technique can have considerable effects on the active bed thickness estimates. It is shown that increasing the upper boundary peak definition from 40% to 60% results in areas of active bed thickness underestimation when there are high rates of suspended sediment and inconsistent laser illumination. Future work should aim to optimize the relationship between the peak definitions and the active bed thickness technique. While the less stringent peak definition for the upper boundary increased active bed thickness in some videos, it is apparent from the plots of Shields Number and active bed thickness that there are trials where the active bed thickness may be further adjusted. While

the automated active bed thickness technique needs to be improved upon, it is of importance that the peaks in the Shields Number and active bed thickness seem to align relatively well throughout the videos. This further validates the use of the Shields number to predict near-bed sediment motion.

Preliminary flux rates show that regular waves in this study had the potential to transport sediment shoreward and ⊡offshore. Visual inspection during the laboratory experiment indicated a net onshore movement of sediment during the regular wave trials, which contradicts multiple regular wave trials' calculated sediment transport rates. All irregular wave trials indicated shoreward sediment transport, agreeing with the visual inspection during the experiments. The discrepancy between observed and calculated sediment transport rates within regular wave trials indicates that future work must continue to improve the automated active bed thickness prediction technique. Additional sensitivity analysis should be performed to assess the effect of post-processing filters and time averaging on PIV derived velocities. Improving estimates of the cnoidal Ursell number through the application of various theoretical models may provide more insight onto the relationship between the Ursell number and sediment transport. Potential theoretical models to consider include the Korteweg-de Vries, Benjamin-Bona-Mahony, Boussinesq, and Improved Boussinesq models (Dingemans 1997). In addition to assessing the various cnoidal models, a comparison between the Ursell number and the duration of critical shear stress exceedance will be completed. This relationship may provide better insight into the relationship between the dimensionless parameters and sediment transport in the nearshore.

REFERENCES

Adrian, R. J., and J. Westerweel. 2011. *Particle image velocimetry*. Cambridge University Press.

Barnes, D., C. Tarragon, L. Davoli, and E. Palmieri. 2015. Coastal Vulnerability Analysis Along the Coast of Pescara (Adriatic Sea, Central Italy). *Coastal and beach erosion: Processes, adaptation strategies and environmental impacts*. Nova Science Publishers, Inc.

Buffington, J. M. 1999. The legend of A. F. shields. *Journal of Hydraulic Engineering*, *125*(4), 376–387. https://doi.org/10.1061/(asce)0733-9429(1999)125:4(376)

Dean, R. G., and R.A. Dalrymple. 2002. *Coastal processes with engineering applications*. Cambridge University Press.

Dingemans, M. W. 1997. *Water wave propagation over uneven bottoms*. World scientific.

Dronkers, J. 2005. *Dynamics of coastal systems (Vol. 25, Ser. Advanced Series on Ocean Engineering)*. World Scientific.

Fenton, J. D. 1998. The Cnoidal Theory of Water Waves. J. B. Herbich (Ed.), *Developments in Offshore Engineering* (pp. 1–32).

Hedges, T. S. 1995. Regions of validity of analytical wave theories. *Proceedings of the Institution of Civil Engineers - Water, Maritime and Energy*, *112*(2), 111–114. https://doi.org/10.1680/iwtme.1995.27656

Mariño-Tapia, I. J., P.E. Russell, T.J. O'Hare, M.A. Davidson, and D.A. Huntley. 2007. Cross-shore sediment transport on natural beaches and its relation to sandbar migration patterns: 1. field observations and derivation of a transport parameterization. *Journal of Geophysical Research*, *112*(C3). https://doi.org/10.1029/2005jc002893

Masselink, G., M.J. Austin, T.J. O'Hare, and P.E. Russell. 2007. Geometry and dynamics of wave ripples in the nearshore zone of a coarse sandy beach. *Journal of Geophysical Research*, *112*(C10). https://doi.org/10.1029/2006jc003839

Ostrowski, R. 2018. Influence of wave shape on sediment transport in coastal regions. *Archives of Hydro-Engineering and Environmental Mechanics*, *65*(2), 73–90. https://doi.org/10.1515/heem-2018-0006

Raffel, M., C.E. Willert, F. Scarano, C.J. Kähler, S.T. Wereley, and J. Kompenhans. 2018. *Particle image velocimetry: A practical guide*. Springer.

Roulund, A., J. Sutherland, D. Todd, and J. Sterner. 2016. Parametric equations for shields parameter and wave orbital velocity in combined current and irregular waves. *Scour and Erosion*. https://doi.org/10.1201/9781315375045-37

Shields, A. 1936. ''Application of similarity principles and turbulence research to bed-load movement.''Hydrodynamics Laboratory Publ.No. 167, W. P. Ott, and J. C. van Uchelen, trans., U.S. Dept. of Agr.,Soil Conservation Service Cooperative Laboratory, California Institute of Technology, Pasadena, Calif.

Stachurska, B., and R. Staroszczyk. 2019. Laboratory study of suspended sediment dynamics over a mildly sloping sandy seabed. *Oceanologia*, *61*(3), 350–367. https://doi.org/10.1016/j.oceano.2019.01.006

Svendsen, I. A. 2006. *Introduction to nearshore hydrodynamics*. World Scientific Publishing.

Thielicke, W., and R. Sonntag. 2021. Particle image velocimetry for MATLAB: Accuracy and enhanced algorithms in PIVlab. *Journal of Open Research Software*, *9*(1), 12. https://doi.org/10.5334/jors.334

Thielicke, W., and E.J. Stamhuis. 2014. PIVlab – towards user-friendly, affordable and accurate digital particle image velocimetry in Matlab. *Journal of Open Research Software*, *2*. https://doi.org/10.5334/jors.bl

Valdenarro, R. B. 2020. *Population geography*. Delve Publishing.